processes

MDPI

Article

$CsPbBr_3$ Films Grown by Pulsed Laser Deposition: Impact of Oxygen on Morphological Evolution and Properties

Marcella Marra [1,†], Chiara Provenzano [2,†], Maura Cesaria [1,*], Rosella Cataldo [1], Anna Grazia Monteduro [1] and Anna Paola Caricato [1,*]

[1] Department of Mathematics and Physics "Ennio De Giorgi", University of Salento, 73100 Lecce, Italy; marcella.marra@unisalento.it (M.M.); rosella.cataldo@unisalento.it (R.C.); annagrazia.monteduro@unisalento.it (A.G.M.)
[2] Department of Engineering of Innovation, University of Salento, 73100 Lecce, Italy; chiara.provenzano@unisalento.it
* Correspondence: maura.cesaria@unisalento.it (M.C.); annapaola.caricato@unisalento.it (A.P.C.)
† These authors contributed equally to this work.

Abstract: Among all the inorganic perovskites, cesium lead bromide ($CsPbBr_3$) has gained significant interest due to its stability and remarkable optoelectronic/photoluminescence properties. Because of the influence of deposition techniques, the experimental conditions that play a key role in each need to be addressed. In this context, we present $CsPbBr_3$ films grown by pulsed laser deposition (PLD) and discuss the impact of oxygen stemming from their growth under a reduced vacuum, i.e., as the background atmosphere, rather than from post-growth exposure. In detail, stoichiometric mechano-chemically synthesized targets were prepared for deposition by nanosecond-PLD (λ = 248 nm, τ = 20 ns, room temperature, fluence of 1 J/cm^2) to produce slightly Br-deficient $CsPbBr_3$ films under different background pressure conditions ($P_0 = 10^{-4}$, 10^{-2} Pa). The characterization results suggest that the presence of oxygen during the deposition of $CsPbBr_3$ can advantageously passivate bromide-vacancy states in all the film thicknesses and reduce losses from emissions. Overall, our findings shed light on the critical role of oxygen, under conditions in which we ruled out other effects related to air exposure, and provide valuable guidelines for potential applications in various optoelectronic devices.

Keywords: $CsPbBr_3$ halide perovskite; PLD technique; oxygen incorporation during growth; bromine vacancies

check for updates

Citation: Marra, M.; Provenzano, C.; Cesaria, M.; Cataldo, R.; Monteduro, A.G.; Caricato, A.P. $CsPbBr_3$ Films Grown by Pulsed Laser Deposition: Impact of Oxygen on Morphological Evolution and Properties. *Processes* **2023**, *11*, 2514. https://doi.org/10.3390/pr11092514

Academic Editor: Prashant K. Sarswat

Received: 15 June 2023
Revised: 12 August 2023
Accepted: 17 August 2023
Published: 22 August 2023

Copyright: © 2023 by the authors. Licensee MDPI, Basel, Switzerland. This article is an open access article distributed under the terms and conditions of the Creative Commons Attribution (CC BY) license (https://creativecommons.org/licenses/by/4.0/).

1. Introduction

Although metal halide perovskites (MHPs) were discovered in the 19th century and were intensely studied for their magnetic and optoelectronic properties in the late 20th century, the last decade has seen a surge in interest in these materials. This interest is due to their attractive semiconductor traits, including their direct tunable bandgaps, strong light absorption, relatively small and balanced electron/hole effective masses, and defect tolerance. The relevant flexibility to independently and synergically tune their structural, optical, and electronic properties using stable inorganic rather than hybrid organic–inorganic MHP members suggests outstanding promise for various applications. Additionally,the readily accessible synthesis of high-quality crystals and films enables a facile structure–property correlation and rapid device prototyping/optimization [1]. Among inorganic MHPs, the outstanding optical properties of cesium lead halide perovskites have made them a prominent material in optoelectronics, where $CsPbBr_3$ stands out for its remarkable photo-luminescence properties, including its high photo-luminescent quantum yield, narrow-band emission, and tunable band-gap. These properties show significant potential in various fields, such as photovoltaics, light-emitting diodes, photo-detectors, lasers, field effect transistors, and ionizing radiation detectors [2].

However, the performance of $CsPbBr_3$ is highly dependent on the deposition technique used and understanding/optimizing the fabrication process is challenging but critical for successful device integration and characterization [3,4].

A wide range of approaches is already used for depositing high-quality inorganic perovskite films, such as solution-based methods and dry vacuum methods [5,6], spin-coating [7,8], hot injection [9], solvo-thermal synthesis [10,11], room-temperature precipitation [7], low-temperature solution growth [12], Bridgman growth [13], chemical vapor deposition (CVD) [14], vacuum dual source thermal evaporation [15,16], and pulsed laser deposition (PLD) [17,18].

Although solution-based methods for growing perovskite nanocrystals and films may be inexpensive, the practical disadvantages include the use of toxic chemicals, solubility in different solvents, the formation of multiple Cs-Pb-Br compositions, the numerous processing steps involved in the manufacturing process, and the complex and time-consuming protocols.

Among dry vacuum-assisted methods, although vacuum thermal evaporation represents an interesting pathway for growing perovskite films, its application is critical because of the multiple evaporation sources with different evaporation rates that demand careful calibration of the geometry, distances, and temperatures [16].

An intriguing possibility to overcome the limitations of thermal evaporation in depositing multi-elemental materials is the unique capability of the PLD vacuum-assisted technique to transfer the stoichiometry and allow fine control over the thickness, phase, and morphology [19–21]. These aspects were investigated recently by the authors, who discussed the practical consequences of the uneven masses of Cs, Pb, and Br, which can produce products such as Br-deficient $CsPbBr_3$ films [3,4]. The impact of specific working conditions (time aging, thermal heating, and exposure to high relative humidity) on PLD-deposited $CsPbBr_3$ films [22] inspired by the oxygen-induced passivation of Br vacancies at the air–$CsPbBr_3$ interface that boosts photoluminescence was also explored [23–25]. Indeed, in the literature, it is reported that Br-vacancy defects act as non-radiative recombination shallow trap-centers, meaning photoluminescence quenching states [23,26,27]. The role of oxygen physisorption under air exposure in favoring/suppressing emission from $CsPbBr_3$ due to additional electron acceptor states able to passivate the Br non-radiative trap states [23] is still debated. Indeed, ambiguous literature results show the contribution from the manufacturing technique, crystalline nature, aging/storing procedure, exposure conditions to air, and more [28]. Unlike our early investigation carrying out PLD growth under high vacuum conditions (background pressure of $\sim 10^{-5}$ Pa) [3], in this paper we present recent results on the potential of the PLD technique for depositing $CsPbBr_3$ films under varying background pressures, i.e., the oxygen background conditions varied during growth rather than post-growth exposure causing different environment conditions. This point is particularly interesting because the photoluminescence (PL) emission intensity from $CsPbBr_3$ crystals was demonstrated to increase remarkably ($\sim$60 times) by changing the surrounding atmosphere from vacuum ($\sim 4.7 \times 10^{-4}$ Torr) to air [23]. For comparison, in our experiments, we set a background pressure $P_0 = 2 \times 10^{-4}$ Pa or 2×10^{-2} Pa and demonstrate that such growth conditions improve the spectral stability of the samples, which exhibit slight changes over a few days following their preparation and retain morphological and optical stability over very long periods (monitoring was prolonged over nearly two months).

The underlying reasoning of our experiments aimed to account for the formation of Br vacancies, which are favored by the light mass of Br as compared to Pb and Cs during PLD deposition, and the role of Br vacancies [4]. They lead to bond breakage and unpaired electrons in Pb and introduce shallow trap states at the bottom of the conduction band minimum that, due to their energy location, preferentially trap charge carriers and give rise to non-radiative recombination. Bromine vacancies, with a formation energy lower than interstitial or anti-site defects, are the preferred locations for O_2 adsorption compared to the Br-defect-free $CsPbBr_3$ surface. In practice, the physisorption of O_2 at the location

of the Br vacancy is reported to effectively reduce the density of trap states associated with Br vacancies [23]. Under our experimental conditions, this effect was induced during the growth rather than due to post-growth physisorption of oxygen species. As will be discussed, the refinement of the exciton peak evidenced by optical characterization supports this hypothesis, i.e., the oxygen passivation of the Br vacancies during growth for improving the photostability of PLD-deposited $CsPbBr_3$ films. Notably, the high optoelectronic quality of $CsPbBr_3$ is strictly allowed by a high tolerance to defects due to the fact that, despite the occurrence of point defects, the dominant defects only introduce shallow transition levels, which are not usually carrier trapping centers [27]. Hence, unlike other perovskite materials, $CsPbBr_3$ does not suffer from the relevant impact of the F-centers [29]. Therefore, the interplay between oxygen incorporation and the occurrence of Br vacancies is discussed to provide experimental guidelines to deposit functional $CsPbBr_3$ films by PLD.

2. Materials and Methods

2.1. Preparation of the $CsPbBr_3$ Ablation Targets

The target material used for the PLD experiments was obtained by the all-solid-state mechanochemical synthesis approach as comprehensively detailed elsewhere [3,4]. Briefly, the binary CsBr and $PbBr_2$ precursor powders (purchased from Chempur, 99.9% grade purity) were hand-ground and mixed, in equal molar ratio, for 15–20 min in air and at room temperature to drive the formation of the $CsPbBr_3$ phase. The resulting solid pellets were thermally annealed in an oven at 400 °C for 2 h and, subsequently, at 500 °C for 2 h. As thoroughly described elsewhere [3,4], the stoichiometric 1:1 molar ratio $PbBr_2$: CsBr mixture and the absence of $PbBr_2$ in excess imply that the reaction $3PbBr_2 + Cs_4PbBr_6 \rightarrow 4CsPbBr_3$ may not remove the spurious phase without thermal annealing driving the transformation of the Cs_4PbBr_6 compound to the $CsPbBr_3$ desired phase [4].

2.2. Pulsed Laser Deposition Experiments

PLD experiments were performed by exploiting a typical setup as sketched in Figure 1 consisting of a pulsed excimer laser source, quartz optics to focus the laser beam, a stainless-steel vacuum chamber wherein both a rotating target holder and substrate holder are present, and a pumping system combining rotative and turbo pumps to evacuate the chamber down to the desired vacuum conditions. In our experiments, the PLD setup was equipped with a KrF laser emitting at 248 nm with a pulse width of τ_p = 20 ns. According to the working principle of the PLD approach, a focused KrF pulsed laser beam with given fluence (i.e., energy delivered per pulse and per unit surface) was delivered to the material to be deposited (a mechanochemically synthesized $CsPbBr_3$ target). As a result of the ablation mechanism [30], a highly forwardly peaked plasma plume forms, which includes the species ejected from the target. These, under expansion in the vacuum chamber, are transferred from the target to the substrate where they deposit and enable film growth. In the conventional on-axis PLD configuration, the target and the substrate are parallel to each other and the substrate axis and the plume axis are coaxial (Figure 1). We considered an offset between the substrate axis and plume axis and a rotating substrate to improve film uniformity [4,31].

A series of films were deposited on silica glass substrates using a target of $CsPbBr_3$ synthesized according to the procedure detailed above. The prepared target was mounted on the target holder, which was rotated at the frequency of 1.2 Hz to avoid crater formation. In addition, drilling of the target under irradiation of the focused laser beam was directed at an angle of 45° with respect to the target axis. Silica substrates, washed in acetone and alcohol in an ultrasonic bath for 10 min each, were mounted on the substrate holder and kept at room temperature. The target to substrate distance was set at the values d_{TS} = 3, 4, and 6 cm. Before any deposition, the target surface was cleaned with 1000 laser pulses fired at a repetition rate of 10 Hz.

As detailed in Table 1, the films of interest in this study were deposited in a stainless-steel chamber evacuated down to a background pressure $P_0 = 2 \times 10^{-4}$ Pa or 2×10^{-2} Pa

with laser fluence F = 1 J/cm^2 , repetition rate RR = 2, 5, 10 Hz, and the number of laser shots N_p = 1200, 2000, and 4500. No substrate heating was applied to study nucleation and the growth mechanisms of $CsPbBr_3$ as strictly related to the energetics of PLD and background pressure. Following the PLD depositions, the samples were aged in a plastic box in dark conditions, i.e., avoiding exposure to environmental moisture and light, in between the repeated characterizations. Inspired by the experimental parameters, the deposited samples were named according to the following nomenclature: $CsPbBr_3$ (P_0, d_{TS}, RR) where P_0 is equal to 2×10^{-4} Pa or 2×10^{-2} Pa, d_{TS} is the target-to-substrate distance (d_{TS} = 3, 4, 6 cm), and RR is the repetition rate (RR = 2, 5, 10 Hz). The value of N_p is omitted because the set values of the deposition parameters yielded films with equal thicknesses, that is, t∼120 nm.

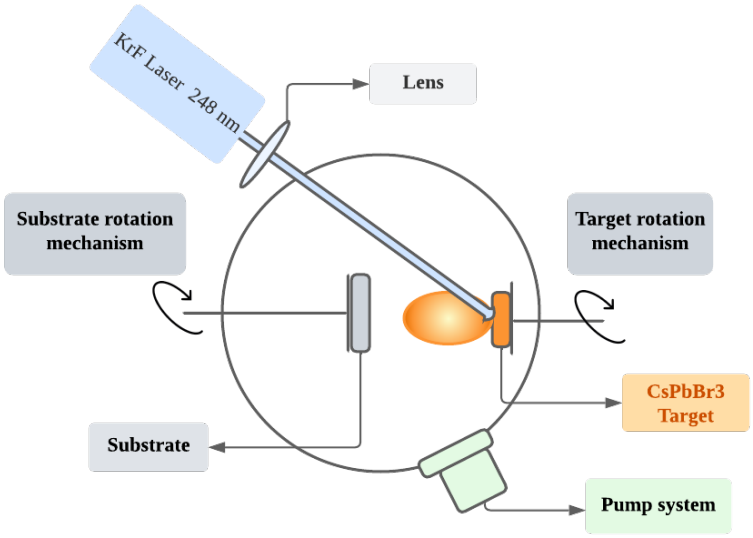

Figure 1. Pulsed laser deposition experimental setup.

Table 1. Nomenclature and details of the deposition parameters for the samples under study. The background pressure is named P_0, the target-to-substrate distance is d_{TS}, the repetition rate is briefly termed RR, and N_P refers to the number of laser pulses.

Sample	P_0 (Pa)	d_{TS} (cm)	RR (Hz)	N_P
$CsPbBr_3$ (2×10^{-4}, 4 cm, 5 Hz)	2×10^{-4}	4	5	2000
$CsPbBr_3$ (2×10^{-2}, 6 cm, 2 Hz)	2×10^{-2}	6	2	4500
$CsPbBr_3$ (2×10^{-2}, 6 cm, 10 Hz)	2×10^{-2}	6	10	4500
$CsPbBr_3$ (2×10^{-2}, 3 cm, 10 Hz)	2×10^{-2}	3	10	1200

3. Characterization Analyses

3.1. X-ray Diffraction (XRD) Analysis

The microstructure of the perovskite films deposited by PLD onto silica substrates was characterized by X-ray diffraction (XRD) analyses carried out using a Rigaku Miniflex diffractometer (Rigatu Company, Tokio, Japan) operating in step-scan mode and employing Cu-Kα X-ray source of wavelength 1.54056 Å. A voltage of 40 kV and a current of 20 mA were set. Data were collected over the angular range 2Θ from 10 to 80 deg, with a 0.020 deg step-size. The Scherrer formula was applied for estimating the size of nanocrystallites, that is, $d = K\lambda/\beta\cos\theta$ where K is a dimensionless shape factor close to unity, λ is the X-ray wavelength, and θ is the Bragg angle.

3.2. Scanning Electron Microscopy (SEM) Analysis

The morphological characterization of the samples was carried out by using a scanning electron microscope (SEM ZEISS Sigma 300 VP, Carl Zeiss, Oberkochen, Germany) working

at an acceleration voltage of 5 kV. The images were acquired in top view configuration by employing a secondary electron detector for low magnification scans and an in-lens detector for high magnification scans.

3.3. Absorption Measurements

The spectral response of the $CsPbBr_3$ films under consideration in this study was investigated by UV–Vis absorbance spectra measured by a PerkinElmer Lambda 900 UV spectrophotometer (PerkinElmer Company, Waltham, MA, USA). Data were acquired over the wavelength interval ranging from 400 nm to 600 nm with a wavelength resolution of 4 nm.

3.4. Digital Image Processing and Statistics

For thresholding and detection of large grains, the plugin of ImageJ/Fiji called StarDist, developed for the detection of irregularly shaped cell/nuclei in microscopy images was applied (https://imagej.net/plugins/stardist, accessed on 1 March 2023).

Because of the sub-optimal contrast of the SEM images due to the charging effects of the glass substrate under exposure to the electron beam, preliminarily to thresholding and segmentation, contrast enhancement was performed using the MEED procedure, which enables the stable convergence of the thresholding algorithms [32].

The MEED-processed SEM images were segmented by setting the versatile (fluorescent nuclei) model of StarDist and adjusting the NMS (non-maximum suppression) post-processing parameters. In this respect, the values of the probability/score threshold and overlap threshold parameters were tuned depending on the image, i.e., higher values of the former parameter yielded fewer segmented objects and the latter parameter allowed us to regulate the overlap between segmented objects. False positives were removed and segmented objects were statistically characterized. With the aim of delving deeper inside the coverage extension, in terms of the occupied areas and the distribution, statistical results were represented by means of box plots and violin plots. Due to the richness of information enclosed in a compact graph, a box plot representation is a powerful visualization tool of sampled continuous data sets [33]. Since it is important to identify features and patterns among groups of data, otherwise not easily evident, many papers address the use of "box plot" in place of bar charts and mean-and-error plots suggesting how to realize this type of graph and to improve the interpretation [34] of data in complex tables [35]. The data of a distribution that can be deducted in box plot are mean, median (the line that crosses the box and corresponds to the value separating the higher half from the lower half of an ordered data set, a population, or a probability distribution), first quartile (Q1, or 25th percentile) and third quartile (Q3, or 75th percentile), outliers, confidence interval, and skewness [36]. The lines extending from Q1 and Q3 are the so-called "whiskers". The quantity I_{QR} = Q3 − Q1 is the interquartile range from which the minimum and maximum values can be calculated, which are not necessarily the smallest or the largest values in the data set. The locations of the fence of the box can be calculated by Q1 − 1.5 × I_{QR} for the lower side and Q3 + 1.5 × I_{QR} for the upper side. The minimum is the smallest value above the lower fence, while the maximum is the largest value below the upper fence of the box. Outside the two fences, the outliers are positioned, usually indicated by graph signs such as crosses (in our case), asterisks, or circles. However, fences are not drawn in the box plot, and they are used to decide outliers, i.e., the minimum and maximum only [35]. An important quantity is the so-called "notch", defined by the formula as CI = 1.58 × $I_{QR}/\sqrt{n}$, where n is the cardinality of the data set, which represents the 95% confidence interval for the median and refers to the narrowing of the box around the median value. Notch is important in evaluating the difference between the medians of two box plots, meaning that if the notches between two box plots do not overlap, then we can be confident that their medians are significantly different from each other. To complement the information provided by box plots showing the full distribution of the data, which is particularly useful when the data distribution is multi-modal (more than one peak), violin

plots were drawn [37]. Visualization of data by violin plot, which is a hybrid form between a box plot and a kernel density plot, foresees a non-parametric density estimation based on a smooth kernel function with a fixed global radius [38]. With respect to a box plot, a violin plot not only summarizes statistics but also adds information on the density of each variable.

4. Results and Discussion

4.1. Compositional, Structural, and Morphological Properties

The elemental analysis performed by XPS on $CsPbBr_3$ samples grown under similar experimental conditions yielded the composition $Cs_{2.1}Pb_1Br_{2.6}$ for the surface layer of the as-deposited films [3,22].

X-ray diffraction (XRD) plots in Figure 2 indicate the occurrence of orthorhombic $CsPbBr_3$ (pdf card # 18-0364) and residuals of the Cs_4PbBr_6 spurious phase (pdf card #73-2478). Indeed, the dominant diffraction lines at 2θ = 15°, 21°, 28°, and 30° can be associated with the lattice planes with orientations (100), (110), (004), and (200), respectively, of the $CsPbBr_3$ orthorombic structure. The presence of the Cs-rich phase is not surprising because $CsPbBr_3$ and Cs_4PbBr_6 tend to coexist: the Cs-rich phase is the spurious phase with the minimum formation energy and Br-deficient composition due to the mass gradient in the plasma plume [4] works against the consumption of the Cs_4PbBr_6 phase by means of the reaction $3PbBr_2 + Cs_4PbBr_6 \rightarrow 4CsPbBr_3$ requiring $PbBr_2$ in excess [3,4].

Notably, the coexistence of both compounds in the $CsPbBr_3$ bulk, thin films, and nanoparticles indicated that the relative amount of chemical elements is not the only parameter dictating the final composition. Indeed, a temperature in the range between 100 °C and 200 °C was found to play a role and hybridization of the Cs_4PbBr_6 and $CsPbBr_3$ phases was observed for low-temperature synthesis conditions that favor small $CsPbBr_3$ nanocrystals [39]. The broadband around 20° is dominated by the contribution of the substrate. The slight variation in intensity of the overall broadband with increasing aging time suggests a contribution from the $CsPbBr_3$ films, due to their equal thickness and the occurrence of a two-fold structure consisting of small and large grains, developing with a columnar-like morphology [3,4]. Therefore, any changes in the overall intensity of the background XRD spectrum can be associated with the evolution and/or increased contribution or refinement of the background small grain family. On the other hand, changes in the peaked features indicate the refinement of the large foreground grains due to the evolution of crystallinity and coalescence/aggregation effects. It can be observed that aging implies an increase in the intensity and a reduction in the FWHM (full width at half maximum) of the dominant planes of the $CsPbBr_3$ phase, with a major effect for the 110 and 200 peaks in the spectrum associated with $CsPbBr_3$ (10^{-2} Pa, 6 cm, 2 Hz) and a minimal variation in the XRD spectrum of $CsPbBr_3$ (10^{-2} Pa, 3 cm, 10 Hz). The measured XRD spectra clearly indicate the formation of the desired $CsPbBr_3$ phase with a crystalline nature despite the room temperature growth. This aspect makes the sample under study well prepared to address the interplay between deposition parameters and the oxygen role/effect in the growing film.

In order to better investigate the correlation between the XRD spectra and morphological properties of the samples under study, a plan-view SEM analysis was performed. In this respect, Figures 3 and 4 show representative areas of the PLD-deposited $CsPbBr_3$ films as a function of the deposition parameters and aging time. Plan-view SEM images reported in Figure 3 refer to the as-deposited samples and let us discuss the role played by the deposition parameters. As can be observed, a bimodal grains distribution with an evident morphological evolution, depending on the deposition conditions, and noticeable differences in terms of the coalescence/agglomeration patterns of the 3D-micrometer-sized islands/grains. Notably, all films were dense and pinhole-free. A general characteristic of all films is the occurrence of a foreground composed of columnar grains ranging in size from tens of nanometers to about 100 nanometers and a compact background consisting of sub-micron sized grains, resulting from high-density nucleation seeds favored by the super-

saturated deposition flux [3,4]. In detail, Figure 3 demonstrates that the $CsPbBr_3$ (10^{-4} Pa, 4 cm, 5 Hz) film exhibits dominance of the foreground as compared to the background and an irregular distribution of domains consisting of coalescing and closely spaced foreground grains with sizes in the order of tens to hundreds of nanometers. On turning from $CsPbBr_3$ (10^{-4} Pa, 4 cm, 5 Hz) to $CsPbBr_3$ (10^{-2} Pa, 6 cm, 2 Hz) and $CsPbBr_3$ (10^{-2} Pa, 6 cm, 10 Hz), a relevant change in the grain distribution can be observed: the size of the foreground grains decreases and coalescence has less impact on their morphology.

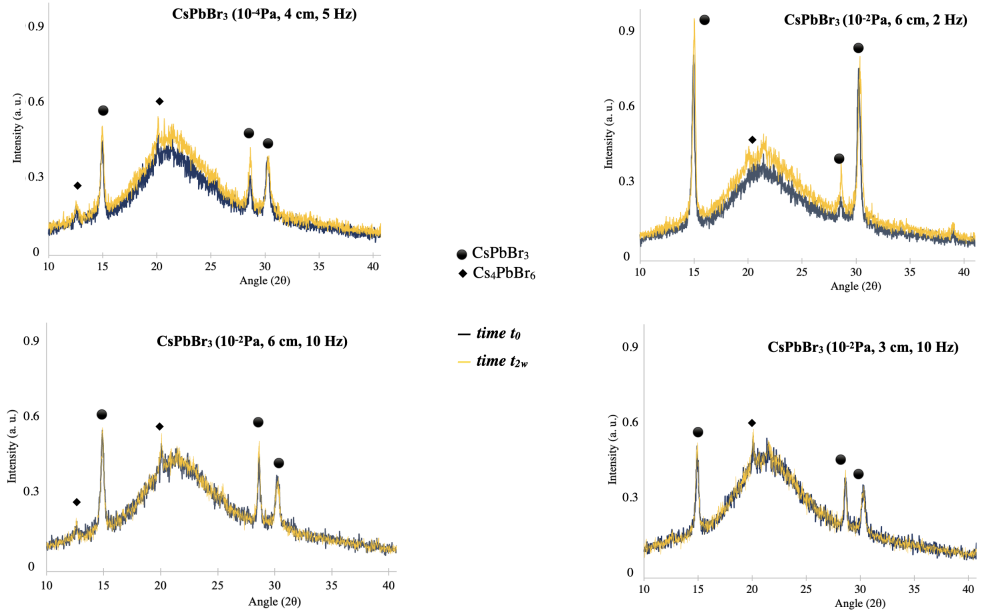

Figure 2. XRD spectra of the samples under study right after deposition (black line, time t_0), after two weeks (light orange line, time t_2w), or after three weeks (dark orange line, time t_3w).

Interestingly, the film morphology disclosed by SEM imaging can account for the interplay between the deposition parameters and the PLD mechanisms. For instance, an increased degree of vacuum works against coalescence events within the plasma plume and yields more energetic deposition flux, meaning energetic deposited species may rearrange through hyperthermally rather than thermally driven kinetics. High and energetic deposition flux is also favored by a decreased target-to-substrate distance. Hence, the interplay between a lower deposition pressure (10^{-4} Pa versus 10^{-2} Pa) and a decreased target-to-substrate distance (4 cm versus 6 cm) can account for the differences between $CsPbBr_3$ (10^{-4} Pa, 4 cm, 5 Hz) and $CsPbBr_3$ (10^{-2} Pa, 6 cm, 2 Hz), because a more intense and more energetic deposition flux favors the initial nucleation of high-density very small nucleation seeds. Hence, film growth evolves through the formation of a small-grained background and subsequent grain growth by migration of the energetic adatoms towards the growing nuclei. Grain growth decreases the relative contribution of the finely grained background with respect to the foreground and favors coalescence/agglomeration effects of the closely spaced nuclei. Under conditions of a reduced degree of vacuum ($P_0 = 10^{-2}$ Pa), nucleation can be promoted by the confinement of the species within the plasma plume and a target-to-substrate distance increase from 4 to 6 cm also contributes to such a trend. Therefore, nucleation during the flying phase of the ablated species within the expanding forwardly peaked plasma plume was expected to result in small grains slightly larger than the nucleation seeds formed due to the supersaturated flux hitting the substrate under vacuum. This picture accounts for and is consistent with the occurrence of a more branched distribution of the foreground grains over the small-grained background for $CsPbBr_3$ (10^{-2} Pa, 6 cm, 2 Hz) and $CsPbBr_3$ (10^{-2} Pa, 6 cm, 10 Hz) with respect to $CsPbBr_3$ (10^{-4} Pa, 4 cm, 5 Hz). Indeed, under high vacuum conditions, grain growth develops preferentially over the substrate where smaller particles are sacrificed at the expense of the growth of

larger islands and their coalescence. Deposition of small nuclei implies that coalescence effects develop among the already-formed small nuclei and the surface migration of the species favors the growth of these small nuclei and the development of networks over the small-grained background, which is directly related to the nucleation seeds induced by supersaturated deposition flux.

The comparison between $CsPbBr_3$ (10^{-2} Pa, 6 cm, 2 Hz) and $CsPbBr_3$ (10^{-2} Pa, 6 cm, 10 Hz) indicates that the deposition rate has no remarkable impact but favors the formation of larger domains (islands) when decreased from 10 to 2 Hz. This experimental finding is in accordance with the literature [40], which discloses the impact of the repetition rate on the growth dynamics of PLD-deposited films. This issue can account for the enhanced intensity of the XRD peaks in the spectrum of $CsPbBr_3$ (10^{-2} Pa, 6 cm, 2 Hz) compared to $CsPbBr_3$ (10^{-2} Pa, 6 cm, 10 Hz).

As a confirmation of the above-indicated role of the target-to-substrate distance and plume confinement related to the increased background pressure, $CsPbBr_3$ (10^{-2} Pa, 3 cm, 10 Hz) exhibits dominance of the finely grained background. The relevant morphological differences with respect to the other ones, in particular, the formation of large and isolated foreground grains, suggest film development driven by Ostwald ripening. That is, due to moderate fluence conditions, small particles are scarified to growth nuclei they can reach by diffusing over a distance limited by their deposition kinetic energy. As a consequence, isolated foreground large grains develop over the small-grained background. Once the foreground grains are fully grown by means of migration of the surrounding small particles, no further growth evolution is expected. This picture can explain the stability observed in the XRD spectrum of $CsPbBr_3$ (10^{-2} Pa, 3 cm, 10 Hz) under aging.

Now the impact of the PLD parameters on the morphological development of the samples under study has been discussed, it is possible to address the role of aging. In the discussion that follows, it should be considered that the presence of defects in perovskite films acts to induce instability in the films [41].

Figure 4 compares the $CsPbBr_3$ films deposited under increased background pressure ($P_0 = 10^{-2}$ Pa) at different times after the deposition, that is, as-deposited (left column) and aged for two weeks (right column). High vacuum conditions are not considered hereafter because our previous discussion demonstrated that the background pressure is the PLD parameter with the most impact on the film morphology.

Notably, the morphology was also investigated over longer aging times, i.e., more than one month after deposition. Since no morphological evolution was observed for aging lasting from two weeks to more than one month, the SEM images shown in Figure 4 are representative of the upper aging threshold above which no data are worthy of consideration, in agreement with the data reported in the XRD spectra.

Two weeks after deposition by PLD, no relevant morphological changes could be observed apart from localized coalescence between closely spaced grains leading to rounding of the foreground and the local connectivity pathways among them (see $CsPbBr_3$ (10^{-2} Pa, 6 cm, 2 Hz) and $CsPbBr_3$ (10^{-2} Pa, 6 cm, 10 Hz)). This evidence indicates a mild rearrangement of the as-deposited morphology and could account for the slight changes in the intensity of the XRD spectra under aging. On the other hand, the sample $CsPbBr_3$ (10^{-2} Pa, 3 cm, 10 Hz) retained its distribution, which consisted of relatively large irregular and isolated foreground grains and can account for the stable XRD spectrum over the sampled aging time.

Definitively, the parameters with the most impact are related to the PLD deposition; in particular, the background oxygen pressure plays the dominant role, and our oxygen-enriched deposition conditions were successful in terms of preparing samples that were morphologically stable over time, apart from slight rearrangements impacting on grain refinement (rounding, localized coalescence/agglomeration, networks) over a few days following deposition.

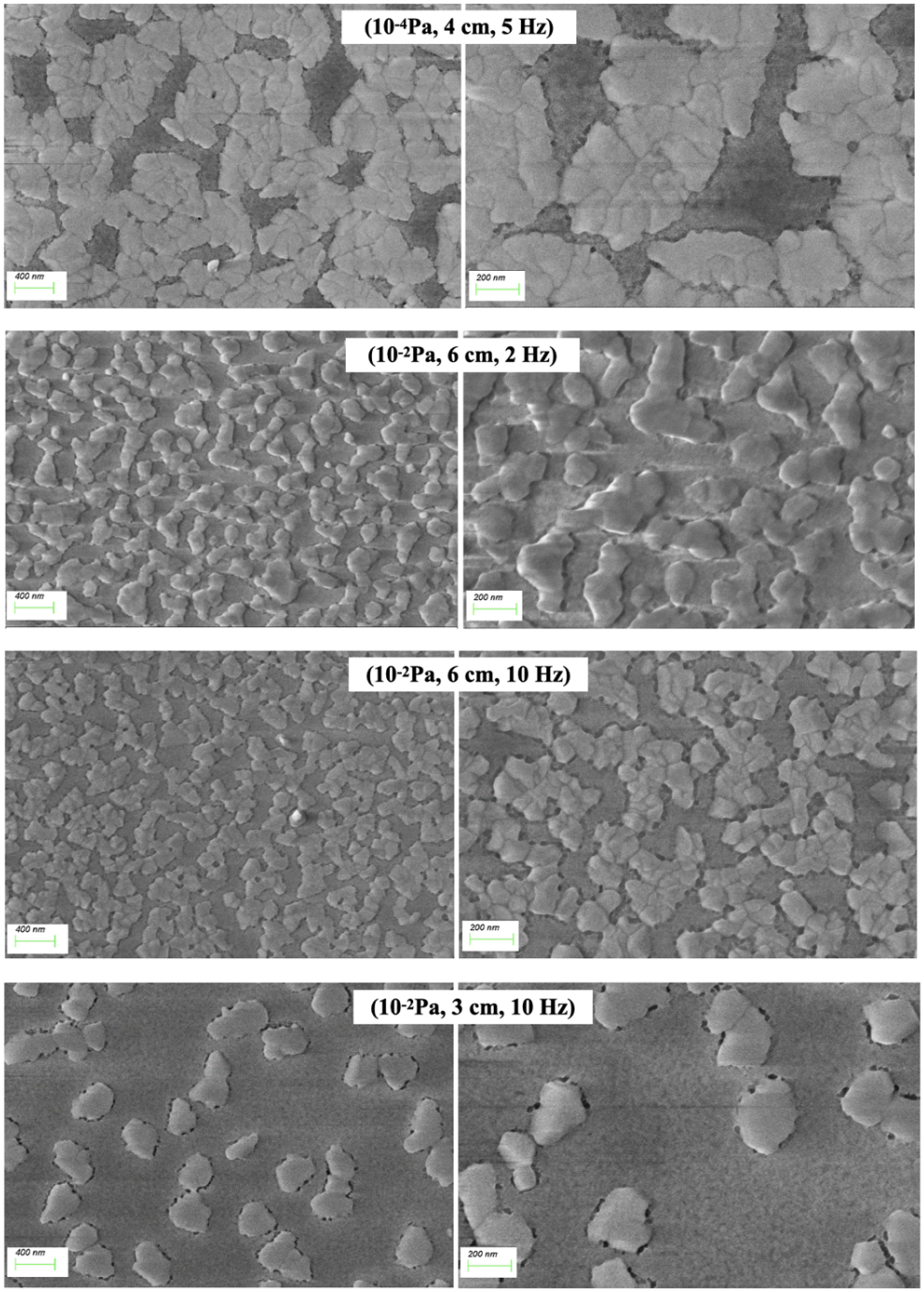

Figure 3. SEM images of the samples of $CsPbBr_3$ (10^{-4} Pa, 4 cm, 5 Hz), $CsPbBr_3$ (10^{-2} Pa, 6 cm, 2 Hz), $CsPbBr_3$ (10^{-2} Pa, 6 cm, 10 Hz), and $CsPbBr_3$ (10^{-2} Pa, 3 cm, 10 Hz) after two weeks from the deposition.

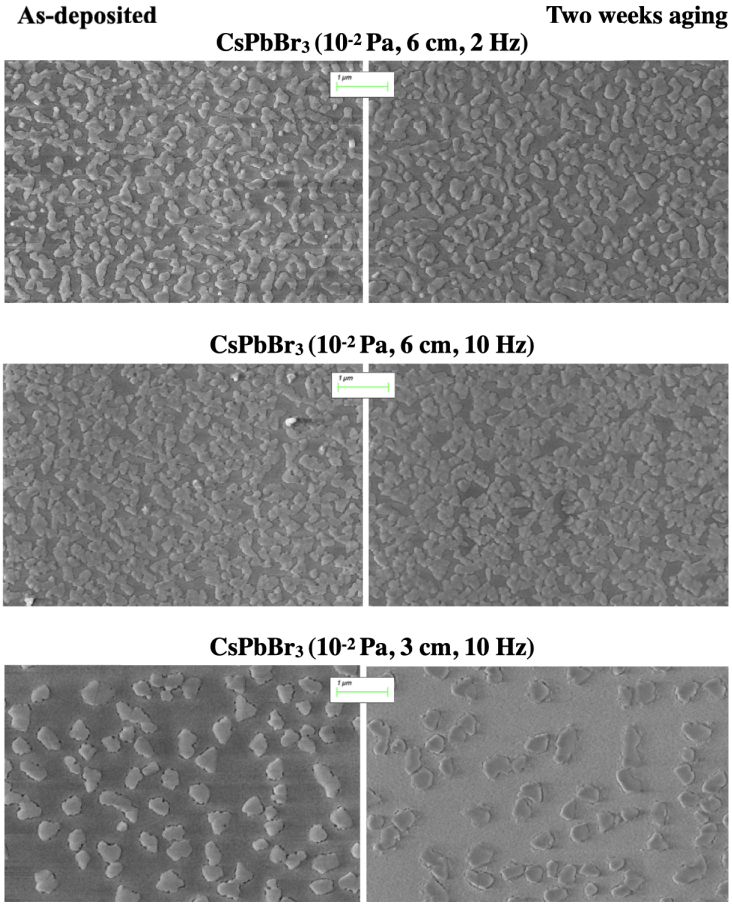

Figure 4. SEM images of the samples of $CsPbBr_3$ (10^{-2} Pa, 6 cm, 2 Hz), $CsPbBr_3$ (10^{-2} Pa, 6 cm, 10 Hz), and $CsPbBr_3$ (10^{-2} Pa, 3 cm, 10 Hz) soon after the deposition (**left**) and after two weeks of aging (**right**).

4.2. Digital Image Processing and Statistics

In order to make the discussion about the impact of the PLD-deposition parameters on the $CsPbBr_3$ films more quantitative, statistical information was carried out based on digital image processing. The left column of Figure 5 shows the segmentation processing of SEM images of the as-deposited samples under consideration in this study. The objects segmented by the StatDist plugin are highlighted by yellow lines and overlapped to the MEED-processed SEM image of the samples listed in Table 1. The right column of Figure 5 reports the area distribution of the segmented objects and lets us observe relevant differences in the size of the sub-classes of grains that are quantitatively indicated by the data listed in Table 2. For each test image, this is in the form of detailed information linked to the number and (the minimum, maximum, and mean) area of the segmented objects (patterns) together with the percentage of coverage, i.e., the percentage of the image area covered by the objects identified during the segmentation phase and associated with the foreground grains. It is immediately clear that the coverage is quite different, on one hand, confirming what is evident based on the visual inspection and, on other hand, that the deposition conditions crucially influence the cluster formations. In particular, the sample $CsPbBr_3$ (10^{-4} Pa, 4 cm, 5 Hz) has a significantly greater maximum coverage and maximum area of clusters than the other samples, which is consistent with grains formed by coalescence of smaller grains. This aspect can be clearly observed by means of the SEM image in Figure 5 and is discussed based on the PLD mechanisms. The minimum percentage of coverage is associated with $CsPbBr_3$ (10^{-2} Pa, 3 cm, 10 Hz), which presents a very enlarged distribution around the mean value, with many area values smaller than the mean area. The representation of the statistical analysis summarized in Table 2 with the

most impact is given in Figure 6, which reports the box plots and the violin plots of the area distributions resulting from the segmentation shown in Figure 5. Figure 6 confirms the differences among the images by pointing out the consistent dissimilarity, especially with respect to $CsPbBr_3$ (10^{-2} Pa, 3 cm, 10 Hz), for which the maximum degree of variation in the segmented areas is registered. The violin plot also clearly indicates that there was no remarkable impact from the repetition rate within the sampled set.

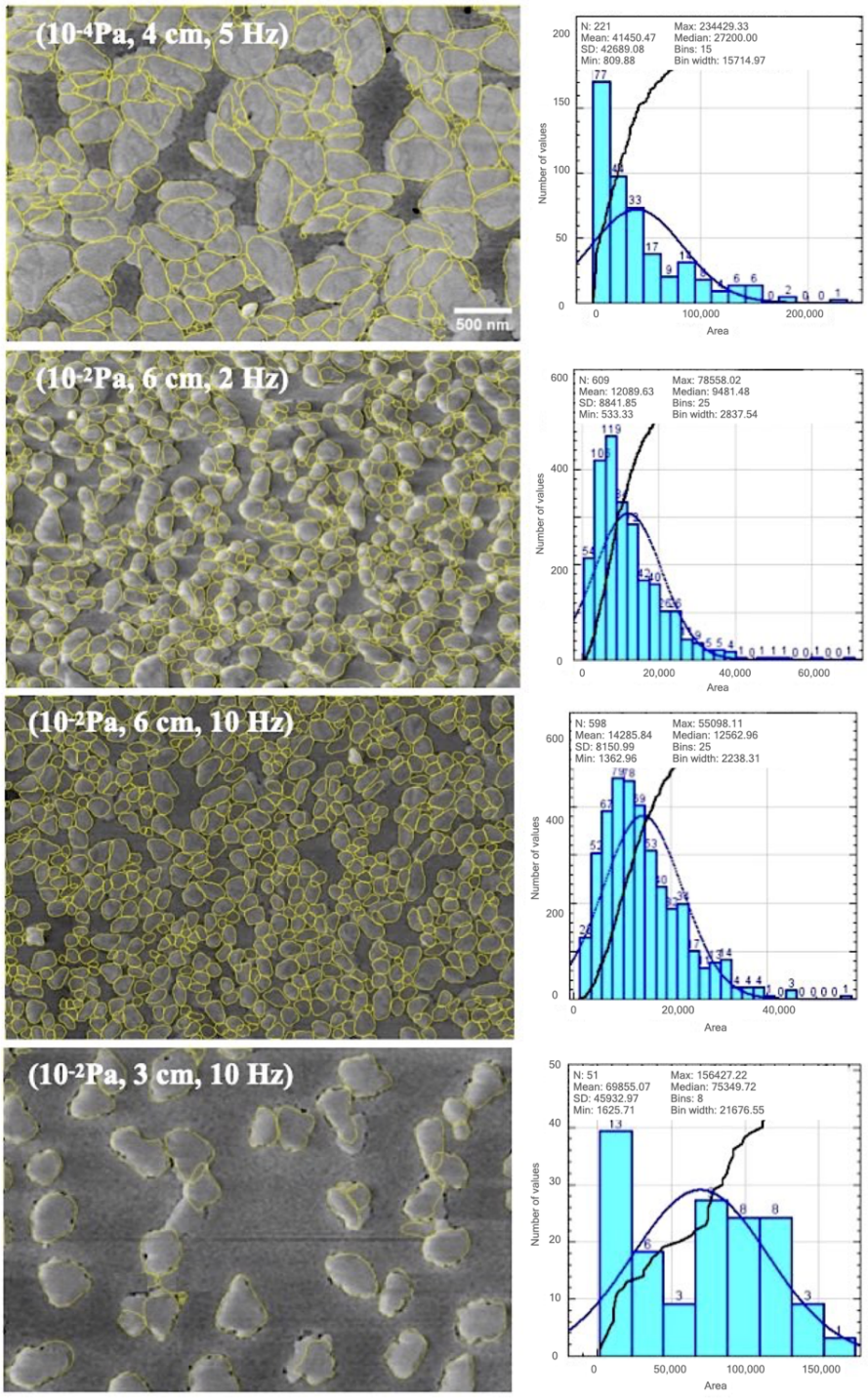

Figure 5. Objects segmented by the StatDist plugin highlighted by yellow lines and overlapped to the MEED-processed SEM image of the samples of $CsPbBr_3$ (10^{-4} Pa, 4 cm, 5 Hz), $CsPbBr_3$ (10^{-2} Pa, 6 cm, 2 Hz), $CsPbBr_3$ (10^{-2} Pa, 6 cm, 10 Hz), and $CsPbBr_3$ (10^{-2} Pa, 3 cm, 10 Hz) listed in Table 2.

Table 2. Information regarding the number and area of the segmented objects, together with the percentage of coverage, for the samples of $CsPbBr_3$ (10^{-4} Pa, 4 cm, 5 Hz), $CsPbBr_3$ (10^{-2} Pa, 6 cm, 2 Hz), $CsPbBr_3$ (10^{-2} Pa, 6 cm, 10 Hz), and $CsPbBr_3$ (10^{-2} Pa, 3 cm, 10 Hz).

	2×10^{-4} Pa	**2×10^{-2} Pa**	**2×10^{-2} Pa**	**2×10^{-2} Pa**
	4 cm, 5 Hz	**6 cm, 2 Hz**	**6 cm, 10 Hz**	**3 cm, 10 Hz**
# of cluster	221	609	598	51
Minimum area (nm^2)	0.8×10^3	0.5×10^3	1.4×10^3	1.6×10^3
Maximum area (nm^2)	2.3×10^5	0.7×10^5	0.6×10^5	1.6×10^5
Mean area (nm^2)	4.1×10^4 $\pm 0.4 \times 10^4$	1.2×10^4 $\pm 0.1 \times 10^4$	1.4×10^4 $\pm 0.8 \times 10^4$	7×10^4 $\pm 4.6 \times 10^4$
Coverage (%)	71.99	57.86	61.45	25.63

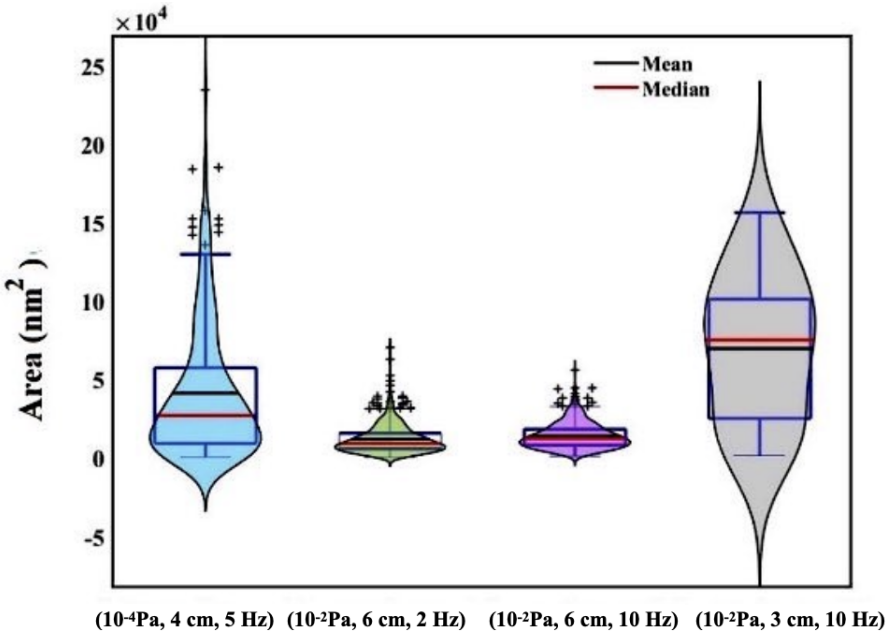

Figure 6. Box plots and violin plots of the area distributions resulting from the segmentation shown in Figure 5.

4.3. Absorbance Properties

Regarding the optical properties of the PLD-deposited $CsPbBr_3$ film under investigation, the UV-Vis absorbance spectra depicted in Figure 7 display a peak at around 505–510 nm for all samples, which is characteristic of the $CsPbBr_3$ composition and can be attributed to the exciton in the vicinity of the optical band gap of $CsPbBr_3$.

The absorption excitonic feature exhibits a more refined shape in the case of the samples of $CsPbBr_3$ (10^{-2} Pa, 6 cm, 2 Hz) and $CsPbBr_3$ (10^{-2} Pa, 6 cm, 10 Hz) and a reduction in the relative intensity of the excitonic peak in the other two cases.

This outcome is consistent with and indicates the improved crystallinity of the foreground grains and/or the larger density of the foreground grains contributing to the signal. Notably, reports in the literature describe the facilitated crystallization of perovskite materials induced by oxygen due to its reducing defects at the interfaces and grain boundaries or within the bulk crystals through diffusion under annealing in atmosphere [42,43].

Indeed, as discussed, growth occurring at $P_0 = 10^{-2}$ Pa not only improves the incorporation of the oxygen in the growing film but also favors nucleation with respect to a higher vacuum background.

In Figure 8, the time evolution of the absorption spectra of the films under study is depicted, following aging periods from one week up to eight weeks. For the reader's guidance, the lines go from lighter to darker over time. On turning from the as-deposited

to the associated aged sample, all samples exhibit a decrease in the absorbance curve with the exception of the sample $CsPbBr_3$ (10^{-2} Pa, 6 cm, 2 Hz) and the stable absorbance signal for aging prolonged from one week to eight weeks. This evidence suggests the structural/morphological refinement of the films over a short aging time, which increases the transparency and is consistent with the slightly enhanced intensity of the XRD spectra following the PLD deposition. The comparison between Figures 7 and 8 increases our understanding of the structural evolution through the refinement of the exciton peak, which becomes more clearly distinguishable with respect to the contribution associated with the band absorption [44]. This evidence demonstrates and confirms that the exciton peak is affected by defects (the reduction in the Br vacancies by oxygen passivation in our case) and disordering (changes in the morphology of the grain boundaries depending on the deposition conditions). Notably, using a deposition pressure higher than the high vacuum commonly used in PLD experiments results in samples with systematically more stable absorbance properties over time. While the photoluminescence measurements are not reported because they are outside of the focus of this paper (the morphological and structural characteristics of $CsPbBr_3$ films depending on the parameters and mechanisms of the PLD technique) and are reported elsewhere [3,4,22], the photoluminescence signal of the $CsPbBr_3$ films under consideration was monitored over time for several months following PLD deposition. This observation confirmed the stable attitude to the emission of green light under aging and is the subject of further investigation. Together, this confirms the view of Br-vacancy saturation with oxygen and suggests a practical recipe to partially overcome the Br deficiency of the PLD-deposited $CsPbBr_3$ films resulting from relevant differences in the atomic mass of the involved elements (Cs, Pb, and Br, which are the lighter species) by oxygen-induced passivation of Br vacancies [23–27]. It should be emphasized that increasing the chamber pressure during growth in a clean atmosphere eliminates the contribution of environmental contaminants compared to exposure in air, which may introduce additional defect states and competitive factors with the passivation of Br states. Therefore, by minimizing the presence of contaminants and controlling the introduction of oxygen, the long-term stability of these devices and their overall performances can be improved.

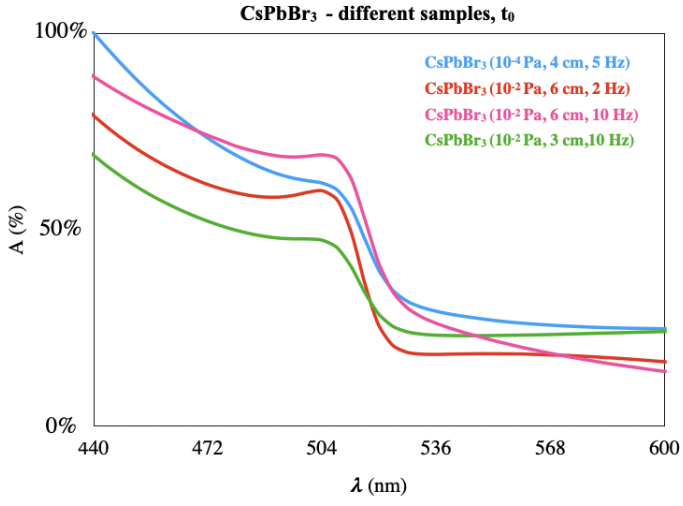

Figure 7. Absorption spectra of the films of $CsPbBr_3$ (10^{-4} Pa, 4 cm, 5 Hz), $CsPbBr_3$ (10^{-2} Pa, 6 cm, 2 Hz), $CsPbBr_3$ (10^{-2} Pa, 6 cm, 10 Hz), and $CsPbBr_3$ (10^{-2} Pa, 3 cm, 10 Hz) right after deposition.

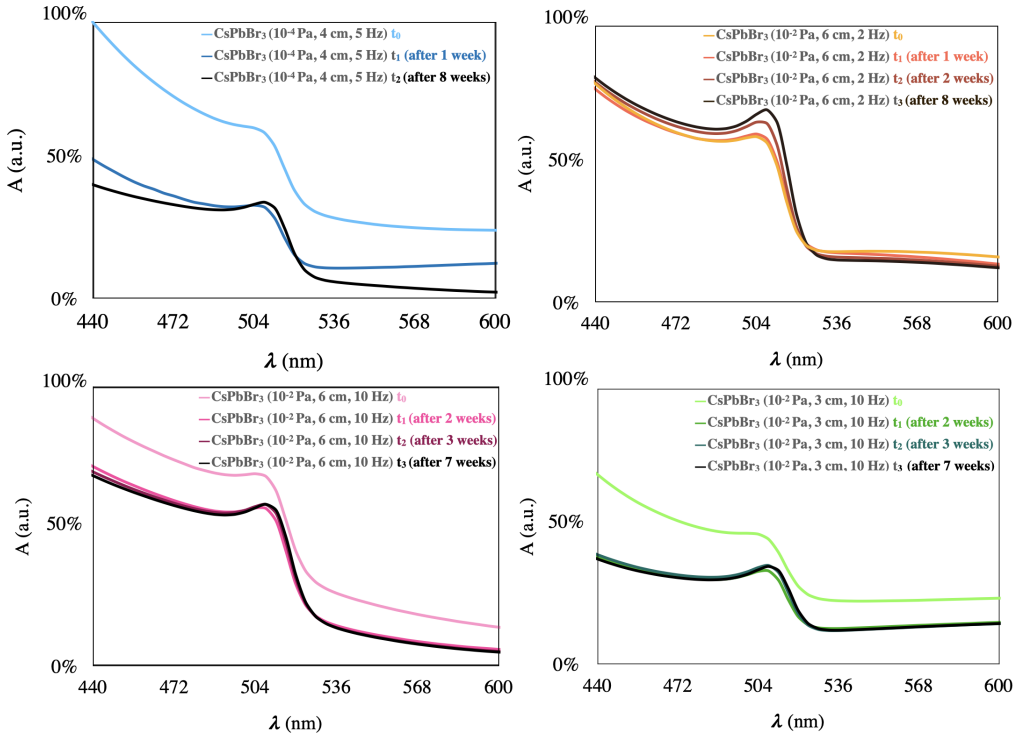

Figure 8. Absorbance spectra of the samples of $CsPbBr_3$ (10^{-4} Pa, 4 cm, 5 Hz), $CsPbBr_3$ (10^{-2} Pa, 6 cm, 2 Hz), $CsPbBr_3$ (10^{-2} Pa, 6 cm, 10 Hz), and $CsPbBr_3$ (10^{-2} Pa, 3 cm, 10 Hz) measured in time: the lightest lines indicate the measurements at time zero and they go from lighter to darker over time.

4.4. Remarks

This study focuses on investigating the potentialities and issues of PLD techniques in terms of deposition strategies. According to the evidence reported in the literature regarding how exposure to oxygen can improve the photoluminescence signal of $CsPbBr_3$ films, we propose an alternative method to ensure that the incorporation of oxygen, whatever its nature, is effective during film growth, rather than being restricted to the surface and depending on the applied treatment. Although out of the scope of our study, the nature of oxygen located in our perovskite films is an interesting aspect to be considered for future studies in relation to the potentialities of PLD in growing functional $CsPbBr_3$ films. Bromine vacancy passivation using oxygen has been identified as an efficient and convenient approach to enhance the photoluminescence signal of $CsPbBr_3$. A literature survey indicates the passivation of Br vacancies through the physisorption of oxygen molecules [23] and oxygen atoms [45]. Unlike molecular oxygen, oxygen atoms are reported to provide better passivation effects due to their stronger interaction with perovskites and their incorporation into the whole film rather than into the surface, which occurs under suitable conditions only. In order to achieve O-passivated rather than O_2-passivated Br vacancies in $CsPbBr_3$, dry-air fabrication/processing was applied in such a way as to dissociate molecular oxygen during the annealing process. In the case of the experiments discussed elsewhere [3], a compositional and binding analysis of $CsPbBr_3$ films grown by PLD under vacuum conditions and subsequently exposed to air demonstrated a O_1s peak signal at (532.5 ± 0.2) eV. This binding energy value indicates adsorbed oxygen in the molecule state [45]. On the other hand, it is worth observing that the composition of the plasma plume generated during a PLD experiment is very complex and several kinds of oxygen species (molecular, atomic, ionic, and excited species) can form in the presence of the oxygen background [46]. For instance, the effective dissociation of oxygen molecules was reported when the plume follows a shockwave-like expansion regime in reactive PLD using oxygen [47]. Therefore, it can be regarded as very likely that both molecular oxygen and oxygen atoms concurred to passivate the Br vacancies in the case of our film. This topic, which is currently under

investigation by XPS analysis and will be the subject of an upcoming paper, is undoubtedly of practical interest to fully assess the potentialities of the PLD technique. In this respect, the O-induced passivation of halide vacancies was found to induce solar cells with a higher efficiency and film stability than O_2-induced passivation [45]. Moreover, the affinity between oxygen species and defects may depend on the perovskite material and preparation protocol.

5. Conclusions

In this study, we present a detailed investigation into the impact of the deposition process in preparing $CsPbBr_3$ thin films using the PLD technique at room temperature. A comprehensive characterization study was carried out, covering various aspects including the structural, compositional, morphological, and optical properties of the grown films. One of the intriguing aspects of our study is the peculiar methodological device we employed, which involved exposing the samples to a higher background pressure during their growth, instead of post-growth exposure to air. The critical reasoning behind our experiments was a search for evidence that the passivation of the Br vacancies is useful in the case of PLD-deposited $CsPbBr_3$ films because, as demonstrated and extensively discussed by the authors elsewhere [3,4], the different masses of the species transferred from the stoichiometric $CsPbBr_3$ target material to the substrate through the expanding plasma plume inherently generate Br vacancies. The morphological evolution of the films under study is discussed as a result of tuning both certain deposition parameters affecting the nucleation density (such as the target-to-substrate distance and number of laser shots) and the background pressure.

This approach is shown to be significant as it has allowed us to enhance the stability of the optical properties of the films over time and to eliminate the contribution of environmental contaminants. Therefore, the promising results can be entirely ascribed to the oxygen contribution introduced in the growing material as a stable constituent.

Our results support the point of view that the saturation of Br vacancies with oxygen and the reduction in competitive factors with the passivation of Br states play a crucial role in improving the long-term stability of the devices and enhancing their overall performance. Moreover, a high background pressure during a PLD process influence both the energy of the ablated species, the nucleation seeds and, consequently, the film growth and properties. This innovative approach has the potential to open up new possibilities for advancements in the field of $CsPbBr_3$ thin films and can contribute to the performance progress of optoelectronic devices based on these materials. One of the most challenging aspects for the practical application of the investigated $CsPbBr_3$ films lies in their potential use as particle detectors. In this context, the presented results seem particularly remarkable due to the luminescence stability produced in $CsPbBr_3$ scintillators, which will be discussed in an upcoming study.

Author Contributions: Conceptualization, M.M., C.P. and M.C.; methodology, M.M. and C.P.; statistical analysis, R.C. and M.C.; morphological and optical analysis, M.M., C.P. and A.G.M.; resources, A.P.C.; data curation, M.C.; writing—original draft preparation, M.M., C.P. and M.C.; editing, M.C. and A.P.C.; supervision, M.C. and A.P.C.; project administration, A.P.C. All authors have read and agreed to the published version of the manuscript.

Funding: This research received no external funding.

Data Availability Statement: Data are available upon request to the authors.

Acknowledgments: A heartfelt acknowledgment is due to Francesca Mancarella for the acquisition of the absorbance spectra.

Conflicts of Interest: The authors declare no conflict of interest.

References

1. Mitzi, D.B. Introduction: Perovskites. *Chem. Rev.* **2019**, *119*, 3033–3035. [CrossRef]
2. Jiang, Y.; Li, B.; Zhang, T.; Shi, Y.; Xu, Q.H. Photoluminescence Mechanisms of All-Inorganic Cesium Lead Bromide Perovskites Revealed by Single Particle Spectroscopy. *Chem. Nanomat.* **2020**, *6*, 327–335. [CrossRef]
3. Cesaria, M.; Quarta, G.; Guascito, M.R.; Mazzeo, M.; Marra, M.; Provenzano, C.; Aziz, M.R.; Martino, M.; Calcagnile, L.; Caricato, A.P. $CsPbBr_3$ deposited by laser ablation: Effects of post-growth aging, oxygen adsorption and annealing on film properties. *Appl. Phys. A* **2022**, *128*, 950. [CrossRef]
4. Cesaria, M.; Mazzeo, M.; Quarta, G.; Aziz, M.R.; Nobile, C.; Carallo, S.; Martino, M.; Calcagnile, L.; Caricato, A.P. Pulsed Laser Deposition of $CsPbBr_3$ Films: Impact of the Composition of the Target and Mass Distribution in the Plasma Plume. *Nanomaterials* **2021**, *11*, 3210. [CrossRef]
5. Zhang, Q.; Yin, Y. All-Inorganic Metal Halide Perovskite Nanocrystals: Opportunities and Challenges. *ACS Cent. Sci.* **2018**, *4*, 668–679. [CrossRef]
6. Soto-Montero, T.; Soltanpoor, W.; Morales-Masis, M. Pressing challenges of halide perovskite thin film growth. *APL Mater.* **2020**, *8*, 110903. [CrossRef]
7. Liu, C.; Cheng, Y.; Ge, Z. Understanding of perovskite crystal growth and film formation in scalable deposition processes. *Chem. Soc. Rev.* **2020**, *49*, 1653–1687. [CrossRef]
8. Teng, P.; Han, X.; Li, J.; Xu, Y.; Kang, L.; Wang, Y.; Yang, Y.; Yu, T. Elegant Face-Down Liquid-Space-Restricted Deposition of $CsPbBr_3$ Films for Efficient Carbon-Based All-Inorganic Planar Perovskite Solar Cells. *ACS Appl. Mater. Interfaces* **2018**, *10*, 9541–9546. [CrossRef]
9. Parobek, D.; Dong, Y.; Qiao, T.; Son, D.H. Direct Hot-Injection Synthesis of Mn-Doped $CsPbBr_3$ Nanocrystals. *Chem. Mater.* **2018**, *30*, 2939–2944. [CrossRef]
10. Zhai, W.; Lin, J.; Li, C.; Hu, S.; Huang, Y.; Yu, C.; Wen, Z.; Liu, Z.; Fangab, Y.; Tang, C. Solvothermal synthesis of cesium lead halide perovskite nanowires with ultra-high aspect ratios for high-performance photodetectors. *Nanoscale* **2018**, *45*, 21451–21458. [CrossRef]
11. Zhai, W.; Lin, J.; Li, Q.; Zheng, K.; Huang, Y.; Yao, Y.; He, X.; Li, L.; Yu, C.; Liu, C.; et al. Solvothermal Synthesis of Ultrathin Cesium Lead Halide Perovskite Nanoplatelets with Tunable Lateral Sizes and Their Reversible Transformation into $Cs4PbBr_6$ Nanocrystals. *Chem. Mater.* **2018**, *30*, 3714–3721. [CrossRef]
12. Rakita, Y.; Kedem, N.; Gupta, S.; Sadhanala, A.; Kalchenko, V.; Böhm, M.L.; Kulbak, M.; Friend, R.H.; Cahen, D.; Hodes, G. Low-temperature solution-grown $CsPbBr_3$ single crystals and their characterization. *Cryst. Growth Des.* **2016**, *16*, 5717–5725. [CrossRef]
13. Stoumpos, C.C.; Malliakas, C.D.; Peters, J.A.; Liu, Z.; Sebastian, M.; Im, J.; Chasapis, T.C.; Wibowo, A.C.; Chung, D.Y.; Freeman, A.J.; et al. Crystal Growth of the Perovskite Semiconductor CsPbBr3: A New Material for High-Energy Radiation Detection. *Cryst. Growth Des.* **2013**, *13*, 2722–2727. [CrossRef]
14. Wang, Y.; Guan, X.; Li, D.; Cheng, H.C.; Duan, X.; Lin, Z.; Duan, X. Chemical vapor deposition growth of single-crystalline cesium lead halide microplatelets and heterostructures for optoelectronic applications. *Nano Res.* **2017**, *10*, 1223–1233. [CrossRef]
15. Zhang, L.; Yuan, F.; Dong, H.; Jiao, B.; Zhang, W.; Hou, X.; Wang, S.; Gong, Q.; Wu, Z. One-Step Co-Evaporation of All-Inorganic Perovskite Thin Films with Room-Temperature Ultralow Amplified Spontaneous Emission Threshold and Air Stability. *ACS Appl. Mater. Interfaces* **2018**, *10*, 40661–40671. [CrossRef] [PubMed]
16. Lei, J.; Gao, F.; Wang, H.; Li, J.; Jiang, J.; Wu, X.; Gao, R.; Yang, Z.; Liu, S. Efficient planar $CsPbBr_3$ perovskite solar cells by dual-source vacuum evaporation. *Sol. Energy Mater. Sol. Cells* **2018**, *187*, 1–8. [CrossRef]
17. Huang, Y.; Zhang, L.; Wang, J.; Zhang, B.; Xin, L.; Niu, S.; Zhao, Y.; Xu, M.; Chu, X.; Zhang, D.; et al. Growth and optoelectronic application of $CsPbBr_3$ thin films deposited by pulsed-laser deposition. *Opt. Lett.* **2019**, *44*, 1908–1911. [CrossRef]
18. Wang, H.; Wu, Y.; Ma, M.; Dong, S.; Li, Q.; Du, J.; Zhang, H.; Xu, Q. ulsed Laser Deposition of CsPbBr3 Films for Application in Perovskite Solar Cells. *ACS Appl. Energy Mater.* **2019**, *2*, 2305–2312. [CrossRef]
19. Schou, J. Physical aspects of the pulsed laser deposition technique: The stoichiometric transfer of material from target to film. *Appl. Surf. Sci.* **2009**, *255*, 5191–5198. [CrossRef]
20. Cesaria, M. Surface energy and nucleation modes. In *Pulsed Laser Ablation: Advances and Applications in Nanoparticles and Nanostructuring Thin Films*; Pan Stanford Publishing Pte Ltd.: Singapore, 2018; pp. 1–84. [CrossRef]
21. Ameer, Z.; Monteduro, A.; Rizzato, S.; Caricato, A. Dielectrical performance of high-k yttrium copper titanate thin films for electronic applications. *J. Mater. Sci. Mater. Electron.* **2018**, *29*, 7090–7098. [CrossRef]
22. Caricato, A.P.; Moretto, S.; Guascito, M.R.; Quarta, G.; Mazzeo, M.; Favaro, M.; Aziz, M.R.; Provenzano, C.; Marra, M.; Cesaria, M.; et al. High scintillation yield and fast response to alpha particles from thin perovskite films deposited by pulsed laser deposition. *Front. Phys.* **2022**, *10*, 895. [CrossRef]
23. Wang, Y.; Ren, Y.; Zhang, S.; Wu, J.; Song, J.; Li, X.; Xu, J.; Sow, C.H.; Zeng, H.; Sun, H. Switching excitonic recombination and carrier trapping in cesium lead halide perovskites by air. *Commun. Phys.* **2018**, *1*, 96. [CrossRef]
24. Brenes, R.; Guo, D.; Osherov, A.; Noel, N.; Eames, C.; Hutter, E.; Pathak, S.; Niroui, F.; Friend, R.; Islam, M.; et al. Metal Halide Perovskite Polycrystalline Films Exhibiting Properties of Single Crystals. *Joule* **2017**, *1*, 155–167. [CrossRef]
25. Howard, J.; Tennyson, E.; Barik, S.; Szostak, R.; Waks, E.; Toney, M.; Nogueira, A.; Neves, B.; Leite, M. Humidity-Induced Photoluminescence Hysteresis in Variable Cs/Br Ratio Hybrid Perovskites. *J. Phys. Chem. Lett.* **2018**, *9*, 3463–3469. [CrossRef]

26. Shi, H.; Du, M.H. Shallow halogen vacancies in halide optoelectronic materials. *Phys. Rev. B* **2014**, *90*, 174103–174108. [CrossRef]
27. Kang, J.; Wang, L.W. High defect tolerance in lead halide perovskite $CsPbBr_3$. *J. Phys. Chem. Lett.* **2017**, *8*, 489–493. [CrossRef]
28. Girolamo, D.D.; Ibrahim-Dar, M.; Dini, D.; Gontrani, L.; Caminiti, R.; Mattoni, A.; Graetzel, M.; Meloni, S. Dual effect of humidity on cesium lead bromide: Enhancement and degradation of perovskite films. *J. Mater. Chem. A* **2019**, *19*, 12292–12302. [CrossRef]
29. Popov, A.I.; Kotomin, E.A.; Majer, J. Basic properties of the F-type centers in halides, oxides and perovskites. *Nucl. Instrum. Methods Phys. Res. Sect. B Beam Interact. Mater. At.* **2010**, *268*, 3085–3089. [CrossRef]
30. Singh, R.K.; Narayan, J. Pulsed-laser evaporation technique for deposition of thin films: Physics and theoretical model. *Phys. Rev. B* **1990**, *41*, 8843–8859. [CrossRef]
31. Ianno, N.J.; Erington, K.B. Thin films of uniform thickness by pulsed laser deposition. *Rev. Sci. Instrum.* **1992**, *63*, 3525–3526. [CrossRef]
32. Cesaria, M.; Alfinito, E.; Arima, V.; Bianco, M.; Cataldo, R. MEED: A novel robust contrast enhancement procedure yielding highly-convergent thresholding of biofilm images. *Comput. Biol. Med.* **2022**, *151*, 106217. [CrossRef] [PubMed]
33. Kampstra, P. A boxplot alternative for visual comparison of distributions. *J. Stat. Softw. Code Snippets* **2008**, *28*, 1–9. [CrossRef]
34. Williamson, D.F.; Parker, R.A.; Kendrick, J.S. The box plot: A simple visual method to interpret data. *Ann. Intern. Med.* **1989**, *110*, 916–921. [CrossRef] [PubMed]
35. Hu, K. Become competent within one day in generating boxplots and violin plots for a novice without prior R experience. *Methods Protoc.* **2020**, *3*, 64. [CrossRef]
36. Krzywinski, M.; Altman, N. Visualizing samples with box plots. *Nat. Methods* **2014**, *11*, 119–120. [CrossRef]
37. Thrun, M.C.; Gehlert, T.; Ultsch, A. Analyzing the fine structure of distributions. *PLoS ONE* **2020**, *15*, e0238835. .]. [CrossRef]
38. Hintze, J.L.; Nelson, R.D. Violin plots: A box plot-density trace synergism. *Am. Stat.* **1998**, *52*, 181–184. [CrossRef]
39. de Weerd, C.; Lin, J.; Gomez, L.; Fujiwara, Y.; Suenaga, K.; Gregorkiewicz, T. Hybridization of Single Nanocrystals of Cs4PbBr6 and CsPbBr3. *J. Phys. Chem. C* **2017**, *121*, 19490–19496. [CrossRef]
40. Govindassamy, G.A.; Prentice, J.J.; Lunney, J.G.; Eason, R.W.; Mackenzie, J.I. Effect of laser repetition rate on the growth of Sc_2O_3 via pulsed laser deposition. *Appl. Phys. A* **2022**, *128*, 577. [CrossRef]
41. Zhou, Y.; Poli, I.; Meggiolaro, D.; Angelis, F.D.; Petrozza, A. Defect activity in metal halide perovskites with wide and narrow bandgap. *Nat. Rev. Mater.* **2021**, *6*, 986–1002. [CrossRef]
42. Pathak, S.; Sepe, A.; Sadhanala, A.; Deschler, F.; Haghighirad, A.; Sakai, N.; Goedel, K.C.; Stranks, S.; Noel, N.; Price, M.; et al. Atmospheric Influence upon Crystallization and Electronic Disorder and Its Impact on the Photophysical Properties of Organic-Inorganic Perovskite Solar Cells. *ACS Nano* **2015**, *9*, 2311–2320. [CrossRef] [PubMed]
43. Ren, W.; Ng, A.; Shen, Q.; Gokkaya, H.C.; Wang, J.; Yang, L.; Yiu, W.K.; Bai, G.; Djurisič, A.B.; Leung, W.W.; et al. Thermal Assisted Oxygen Annealing for High Efficiency Planar CH3NH3PbI3 Perovskite Solar Cells. *Sci. Rep.* **2014**, *4*, 6752. [CrossRef] [PubMed]
44. Baranowski, M.; Plochocka, P. Excitons in Metal-Halide Perovskites. *Adv. Energy Mater.* **2020**, *10*, 1903659. [CrossRef]
45. Liu, S.C.; Li, Z.; Yang, Y.; Wang, X.; Chen, Y.X.; Xue, D.J.; Hu, J.S. Investigation of Oxygen Passivation for High-Performance All-Inorganic Perovskite Solar Cells. *J. Am. Chem. Soc.* **2019**, *141*, 18075–18082. [CrossRef]
46. Schneider, C.W.; Lippert, T. PLD plasma plume analysis: A summary of the PSI contribution. *Appl. Phys. A* **2023**, *129*, 138. [CrossRef]
47. Sambri, A.; Christensen, D.; Trier, F.; Chen, Y.; Amoruso, S.; Pryds, N.; Bruzzese, R.; Wang, X. Plasma plume effects on the conductivity of amorphous-$LaAlO_3/SrTiO_3$ interfaces grown by pulsed laser deposition in O_2 and Ar. *Appl. Phys. Lett.* **2012**, *100*, 231605. [CrossRef]

Disclaimer/Publisher's Note: The statements, opinions and data contained in all publications are solely those of the individual author(s) and contributor(s) and not of MDPI and/or the editor(s). MDPI and/or the editor(s) disclaim responsibility for any injury to people or property resulting from any ideas, methods, instructions or products referred to in the content.